Nanoscale

PAPER

View Article Online
View Journal | View Issue

Cite this: *Nanoscale*, 2022, **14**, 12692

Combined spin filtering actions in hybrid magnetic junctions based on organic chains covalently attached to graphene†

Pascal Martin, [a] Bruno Dlubak, *[b] Richard Mattana,[b] Pierre Seneor,[b] Marie-Blandine Martin,[b] Théo Henner,‡[c] Florian Godel, [b] Anke Sander,[b] Sophie Collin,[b] Linsai Chen,[a] Stéphan Suffit,[c] François Mallet,[c] Philippe Lafarge,[c] Maria Luisa Della Rocca, [c] Andrea Droghetti*[d] and Clément Barraud *[c]

We present a bias-controlled spin-filtering mechanism in spin-valves including a hybrid organic chain/graphene interface. Wet growth conditions of oligomeric molecular chains would usually lead, during standard CMOS-compatible fabrication processes, to the quenching of spintronics properties of metallic spin sources due to oxidation. We demonstrate by X-ray photoelectron spectroscopy that the use of a protective graphene layer fully preserves the metallic character of the ferromagnetic surface and thus its capability to deliver spin polarized currents. We focus here on a small aromatic chain of controllable lengths, formed by nitrobenzene monomers and derived from the commercial 4-nitrobenzene diazonium tetrafluoroborate, covalently attached to the graphene passivated spin sources thanks to electroreduction. A unique bias dependent switch of the spin signal is then observed in complete spin valve devices, from minority to majority spin carriers filtering. First-principles calculations are used to highlight the key role played by the spin-dependent hybridization of electronic states present at the different interfaces. Our work is a first step towards the exploration of spin transport using different functional molecular chains. It opens the perspective of atomic tailoring of magnetic junction devices towards spin and quantum transport control, thanks to the flexibility of ambient electrochemical surface functionalization processes.

Received 7th April 2022,
Accepted 16th August 2022

DOI: 10.1039/d2nr01917e

rsc.li/nanoscale

Introduction

Spintronic circuits, such as widely distributed Magnetic Random Access Memories,[1,2] have been developed for further integration in CMOS (Complementary Metal Oxide Semi-conductor) technologies[3] as well as for post-CMOS visions, such as low-power spin-logic, stochastic and neuromorphic computing.[4–7] Progress along these directions requires optimized material platforms not only to enhance device performances, but, at the same level of importance, also to bring unprecedented functionalities.

Organic, uni-, bi- and tri-dimensional materials have been heralded as promising venues[8–11] for spintronics because of their atom-by-atom tunable physical properties. To date, several works have successfully demonstrated spin transport through these systems in hybrid spin-valve devices.[10,12–15] However only a limited number of organic compounds among the virtually infinite library has been explored for applications proving multifunctionality.[10,16,17] Integrating very diverse molecules into spintronics devices stable under ambient conditions is indeed a difficult technological task. Chemical processes such as electrochemical grafting[18,19] or self-assembly of monolayers[20–22] would in principle represent viable approaches. However, the required wet conditions or the exposure to air during device fabrications processes leads to the oxidation of spin-source electrode materials, such as Ni, Co, Fe and their alloys, thus quenching the spin polarization properties and disrupting device performances. Fabrication protocol has been then developed to circumvent this issue.[23] In this article, we propose an alternative approach to introduce electrochemical grafting processes in spintronics devices. We use a graphene layer to protect metallic electrodes against oxidation and preserve thus their capabilities to deliver a spin-polarized current. Nitrobenzene oligomers are then covalently attached onto graphene *via* a direct C–C bond by electrochemical means demonstrating highly reproducible atomic

[a]*Université Paris Cité, Laboratoire ITODYS, CNRS, UMR 7086, 75013 Paris, France*
[b]*Unité Mixte de Physique, CNRS, Thales, Université Paris-Saclay, 91767 Palaiseau, France. E-mail: bruno.dlubak@cnrs-thales.fr*
[c]*Université Paris Cité, Laboratoire Matériaux et Phénomènes Quantiques, CNRS, UMR 7162, 75013 Paris, France. E-mail: clement.barraud@u-paris.fr*
[d]*School of Physics and CRANN, Trinity College, Dublin 2, Ireland*

†Electronic supplementary information (ESI) available. See DOI: **https://doi.org/10.1039/d2nr01917e**

‡Previously based at Unité Mixte de Physique, CNRS, Thales, Université Paris-Saclay, 91767 Palaiseau, France.

scale crafting of spintronics transport properties. In particular, we realize and fully characterize Ni/graphene/nitrobenzene oligomers/Co junctions. The measurements display a bias-controlled sharp switch of the sign of the magnetoresistive signal. This sharp switch is very specific to our new device and does not resemble to any previously reported results in organic spin-valves or magnetic tunnel junctions.[20,24] It is explained as a combined action of the spin-dependent hybridization between the various materials. Although we use a specific oligomer chain, our technological approach can be applied to electrochemically integrate many different families of molecular compounds onto graphene-protected ferromagnetic electrodes. It therefore offers countless possibilities for improving device performances and for harnessing multifunctional behaviors.

Results and discussion

Fabrication details of organic magnetic junctions based on electrografting wet processes

In Fig. 1, the main steps of our technological process are successively detailed. First, the Ni electrode is patterned on a SiO_2/Si wafer using laser lithography and electron beam evaporation. This allows to define Ni lines playing the role of ferromagnetic spin sources in the final structure. In usual magnetic tunnel junction's structures, the barrier material is subsequently grown *in situ* under vacuum, preserving the metallic surface spin states of the underlying magnetic electrode.[14,25] In our approach, the electrografting procedure of organic compounds is a wet process performed in ambient conditions.[26,27] We thus need to protect the Ni surface against degradation. We make use of a large scale CVD graphene passivation layer which is known to be impermeable and thus prevent oxidation of metals.[28,29] The growth of the graphene layers is achieved by transferring the sample in an adapted cold-wall growth reactor CVD system. The Ni lines exposed to C_2H_2, act as a catalyzer for the growth of graphene (see Methods).[28,30,31] This growth process on Ni spin sources results in a continuous few-layer graphene passivation film. Overall, this process leads to the definition of Ni/Gr lines serving as compatible platforms for electrografting. The next step is the chemical functionalization of the Gr/Ni electrode based on the electroreduction of a diazonium salt.[32–34] This process leads to a compact, thin and stable organic film composed of organic chains covalently grafted onto the Gr/Ni substrate.[19] To demonstrate the principle of our approach, we chose the prototypical 4-nitrobenzene diazonium tetrafluoroborate molecule (NBD named NB after electrografting) which is the simplest diazonium salt commercially available. Different past studies report the use of NBD as a benchmark to illustrate the grafting of diazonium salts since the presence of nitrophenyl groups can be characterized by electrochemistry and X-ray photoelectron spectroscopy (XPS).[35–38] Finally, the evaporation of the Co top electrode can be performed following a standard e-beam evaporation process.

The Fig. 2(a) displays the cyclic voltammetry (C–V) of Gr/Ni electrodes in the presence of 4-nitrophenyl diazonium in acetonitrile solution for five cycles. The recorded CV presents a monoelectronic irreversible wave at potential E_p = −0.3 V per SCE. Following that, the first wave disappears and cannot be recovered upon further cycles. The gradual decrease of the current is related to the passivation of the electrode through the grafting of NB radicals onto Gr/Ni surface. This behavior is clearly attributed to the formation of NO_2-phenyl (NB) film over the Gr/Ni electrode as usually reported for graphene surfaces[39] or for standard metallic surfaces.[26,40] Microscopically, each monomer in its radical form is either covalently bonded to the graphene surface locally modifying its hybridization from sp^2 to sp^3 (ref. 32, 34, 38, 39, 41 and 42) or attached to another monomer already grafted to the graphene surface and thus forming oligomeric chains.[43–45]

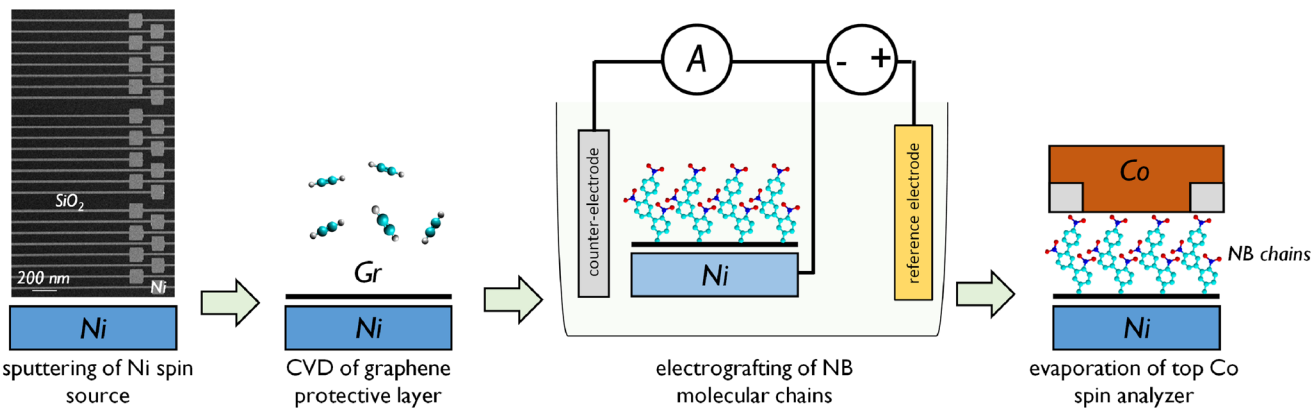

Fig. 1 Technological steps of the fabrication of a functional organic magnetic junction. A 200 nm-thick patterned Ni spin source electrode is deposited by sputtering over a standard Si/SiO_2 substrate. Exposure of C_2H_2 allows the growth of a large-scale graphene layers on top of the Ni electrode to protect it during further chemical processing. The electrografting procedure is then performed to grow amorphous oligomeric organic chains of NB monomers on top of the graphene protected ferromagnetic electrode spin source. Final device integration is carried out to define a magnetic junction where the Gr/NB heterostructure is contacted by two ferromagnetic electrodes (20 nm of Co is chosen as a top electrode).

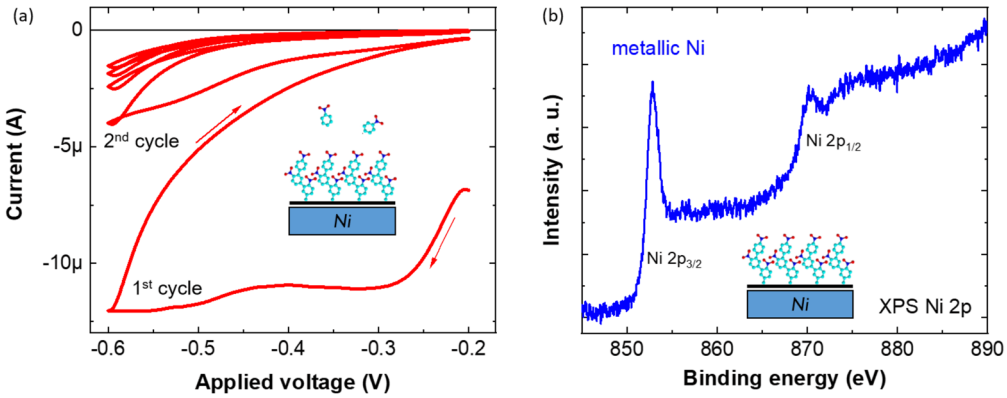

Fig. 2 Electrografting of the molecular chains and preservation of the Ni metallic surface. (a) Cyclic voltammetry of five cycles of Ni/Gr electrodes in a 5 mM NBD solution. Scan rate 100 mV s^{-1}. The chains length can be controlled in a cycle-by-cycle manner allowing tuning the organic barrier thickness in the final structure.[26] Inset: schematics of the growth of the NB chains. Each cycle will generate new radical moieties in the solution. (b) XPS Ni 2p spectrum of Gr/Ni electrodes after the growth of the NB molecular chains. This XPS study confirms the preserved metallic nature of the Ni surface even after electrografting due to the protective nature of the impermeable graphene layer.

This process leads to the coverage of the Gr/Ni electrode by a dense and amorphous film of NB chains as widely described in earlier review.[18] Previous studies demonstrates that this type of organic layers is very compact (*i.e.* strongly limiting atomic diffusion) and thus compatible with solid state electronic devices.[40,43,46–48] Moreover, the number of cycles or the potential window allow to finely tune the thickness of the deposited organic film as determined by AFM or XPS measurements.[26,49,50] Here we focus on a device with an ultrathin NB layers (~1.3 nm) corresponding to 2 cycles of electrografting) to keep the transport process across the organic NB film in the tunneling regime.[26,48]

The main difficulty for implementing surface chemistry of ferromagnetic electrodes for spintronics based on ambient and wet chemistry remains the inescapable degradation of the metallic spin source surface due to the high reactivity of transition metals like Co, Ni or Fe and alloys. Indeed, oxidation occurs at the surface and it is widely known to quench the emerging spin polarization.[51] Few technological solutions were investigated such as the use of oxide materials as electrodes,[52,53] surface pre-cleaning with an appropriate acid[23] or a parallel growth/surface reduction by electrochemistry.[22,54] Graphene protection was also shown to allow preserving a metallic interface in ambient conditions as demonstrated earlier.[28] We investigate here the chemical state of the Ni surface by XPS to assess the pertinence of the proposed graphene passivation after electrografting. As shown in Fig. 2(b), we measure the 2p state of the Ni surface after the grafting process. Strikingly, the XPS study confirm that the Ni surface metallicity is preserved thanks to the graphene protection layer.

Magnetoresistive response of a Ni/graphene/NB/Co magnetic junction

In the following, we present the impact of the integration of the developed stack into a complete spintronic device. Here we focus on the 2-cycles NB film, corresponding to an organic layer thickness of ~1.3 nm to emphasize the effect. As shown on Fig. 1 (SEM image), micrometric Ni/Gr/NB/Co magnetic junction of 5 × 5 μm^2 is fabricated using laser lithography. Here Co (capped by Au) is used as spin analyzer. Fig. 3 shows the typical current–voltage (I–V) characteristics measured at low temperature (T = 2 K). A non-linear behavior with a high (~100 MΩ) zero-bias electrical resistance was observed. The inset shows the calculated differential conductance which has a parabolic trend. All these signatures are typical of tunneling transport between the two ferromagnetic contacts and are in agreement with previous transport experiments performed on the same molecular chains.[46] This demonstrates that the proposed approach indeed allows us to probe transport properties across the organic film. We note that we observe a small rectification (I = +623pA for V = +300 mV and I = −651 pA for V = −300 mV) similar to that found at multilayer graphene/oligomer chain/Au junctions[39] and attributed to the molecule-graphene covalent contact.[55]

The use of spin polarizer and analyzer electrodes in our configuration indeed allows to further probe the spin transport properties across the graphene/NB film. Strikingly, as shown in Fig. 4(a), we measure a magnetoresistive (MR) signal MR = −4% at 2 K, defined as:

$$\mathrm{MR} = \frac{R_{AP} - R_P}{R_P} = \frac{I_P - I_{AP}}{I_{AP}} \quad (1)$$

where R_{AP} (I_{AP}) and R_P (I_P) are the junction's resistance (current) measured in the antiparallel and parallel configurations of the magnetizations respectively. In the experiments, the magnetic field is applied along the Ni electrodes as shown in Fig. 1 which correspond to their magnetization's easy axis as defined during magnetron sputtering deposition: this allows the sharp parallel to antiparallel configurations switches, later observed in MR curves. The magnetizations of both the Ni and Co ferromagnetic electrodes are in-plane as

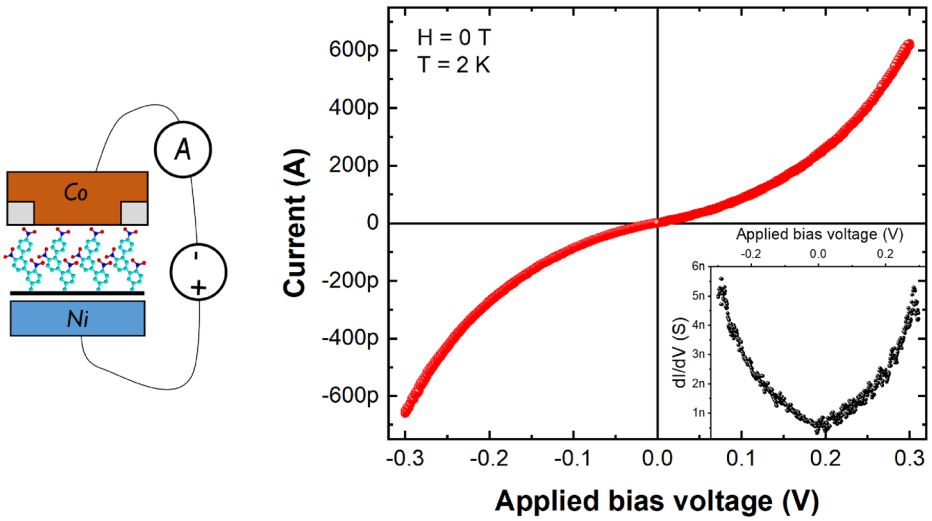

Fig. 3 Charge transport characteristics. *I*–*V* and d*I*/d*V* (inset) of a junction measured across a Ni/Gr/NB (1.3 nm)/Co junction at 2 K revealing high electrical resistance and non-linear tunneling characteristics. A schematic of the measurement configuration is shown on the left.

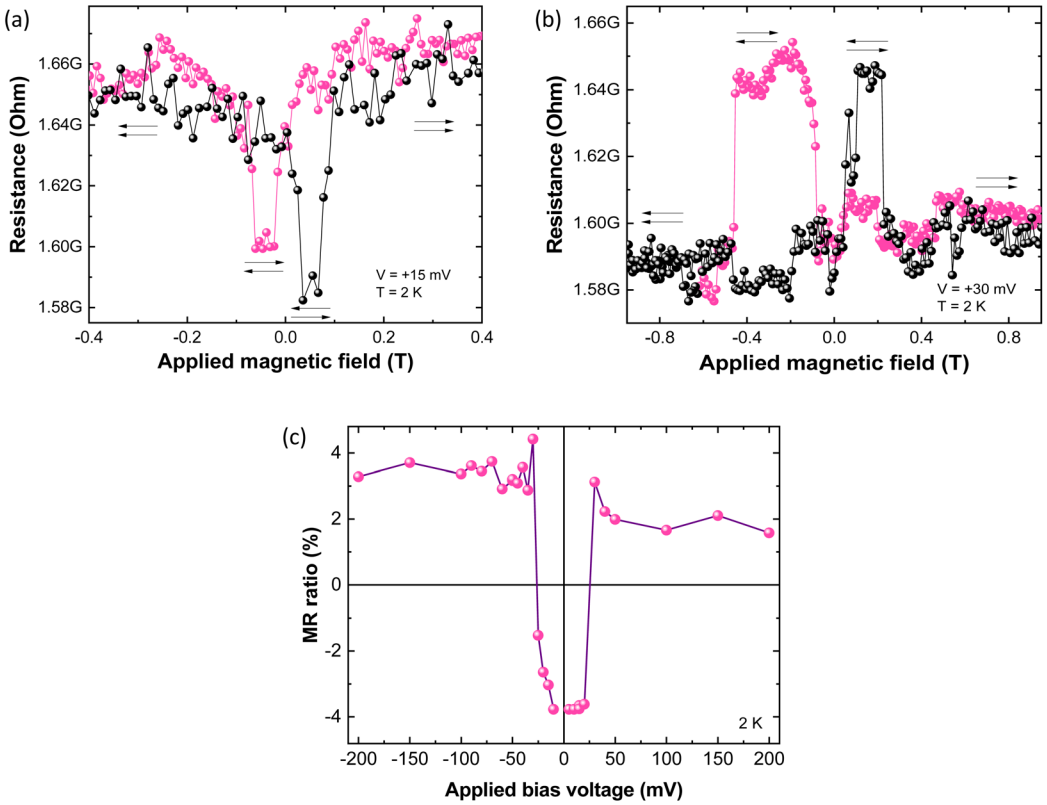

Fig. 4 Magnetoresistive signal and its bias voltage dependence. Magnetoresistance of a NB-based organic magnetic junction. (a) A typical negative MR signal as measured at V = +15 mV (T = 2 K). The pink data points and the black data points represent opposite sweep in magnetic field. (b) The MR signal becomes positive at larger bias voltages as measured at V = +30 mV. (c) The overall spin signal amplitude measured as a function of the applied bias revealing a switch in sign of the spin filtering efficiency across the device.

expected for the given thicknesses, and also already reported in previous publications for similar systems with comparable magnetic electrodes.[28,56] Control devices with only one ferromagnetic electrode made of Au/NB (1.3 nm)/Co were also characterized to verify the absence of any spurious MR effects non-related to spin transport (see Fig. S1†). Also, the observed change of resistance (ΔR ~MΩ) is way above any possible anisotropic magnetoresistance effect.

This demonstrates effective spin transport through the NB-based magnetic junction. Note that the sign of the measured MR (for V = +15 mV) for the low-bias measurements is negative as already reported in Ni/Gr/Al_2O_3/Co magnetic tunnel junctions with Al_2O_3/Co as spin analyzer.[28] Here the extracted emerging spin polarization of the top electrode is defined by the Co/NB hybrid interface and is hence potentially expected to depart from the traditional Al_2O_3/Co spin analyzer due to hybridization effects.[11,15,57]

We thus further characterize the spin transport across our organic heterostructure by measuring the MR response at different bias voltages. Surprisingly, in Fig. 4(b) a full reversal of the spin signal at higher voltage V = +30 mV can be observed. This already shows that the studied system is providing a lever for the manipulation of the sign of the interfacial spin polarizations. In Fig. 4(c) we present a more systematic study of the spin signal amplitude and sign as a function of the applied bias voltage. It appears that two different spin transport regimes are available in the hybrid organic junction. At low bias voltages (+25 mV > V > −25 mV), the junction mimics Ni/Gr/Al_2O_3/Co junctions,[28] with a negative MR. However, at higher bias voltages, we observe an abrupt sign change of the MR signal and we thus deduce that, following the Jullière's formula,[58] one interface has changed its sign in terms of spin polarization. This reversal is observed for both positive and negative bias voltages. This effect is reminiscent of the expected modulation of the spin property due to hybridization at organic/ferromagnetic metal interfaces[15] dubbed "spinterfaces".[59,60] We reveal here an unprecedented extremely sharp control of the sign of the tunneling spin polarization thanks to bias voltage.

Electronic structure of a Ni/Gr/NB/Co junction

To understand spin-filtering across the Ni/Gr/NB/Co junction, we start by carrying out first-principles calculations based on Density Functional Theory (DFT). The simulated device is shown in Fig. 5(a). The molecule is an oligomeric chain composed of three NB units. Three units correspond to a theoretical length of 1.4 nm, which is comparable to the experimental system. The Gr/Ni and the Co electrode are respectively referred to as the bottom and top electrode. The Gr/Ni separation is set equal to the physisorption distance ($d_{Ni/graphene}$ = 3.3 Å)[61] as there is experimental evidence that the CVD graphene passivation layer realized with our approach is physisorbed.[62] Additional details about the system set-up are given in the Methods section.

The junction density of states (DOS) projected over the different material components is presented in Fig. 5(b) for the parallel and antiparallel configurations. We set Ni to have a fixed magnetization, while we switch the direction of Co. Spin-up and spin-down electrons coincide with the Ni majority and minority electrons. A finite spin polarization is induced on graphene *via* proximity with the Ni 3d orbitals as previously reported.[62–64]

Looking in detail at the oligomer chain, we find that, the lowest unoccupied molecular orbital (LUMO) is almost entirely localized on the N and O atoms of the top NB unit, which is in direct contact with the Co electrode. As shown in a previous study,[42] a strong interaction is present between the metallic top electrode and the NB film due to the presence of reactive moieties such as NO_2 in the organic film. Thus, the molecule is chemisorbed *via* the top NO_2 group onto the Co electrode. Its DOS (black line in Fig. 5(b)) is broadened in energy into a resonance and, moreover, is spin-split owing to the hybridization with the Co d orbitals. A similar result was found in a previous review addressing molecules hybridized with Ni surfaces.[11] The LUMO resonance for one spin channel is low in energy and the tail of its DOS crosses the Fermi energy E_F, whereas the LUMO for the other spin channel remains higher in energy separated by about 0.3 eV. As a result, the LUMO acts effectively as a metallic spin-filter (*i.e.* transmitter) state at E_F.[15] Notably, the LUMO spin-polarization at E_F is opposite with respect to that of the Co electrode. We can therefore consider the NO_2 group together with Co as a new effective elec-

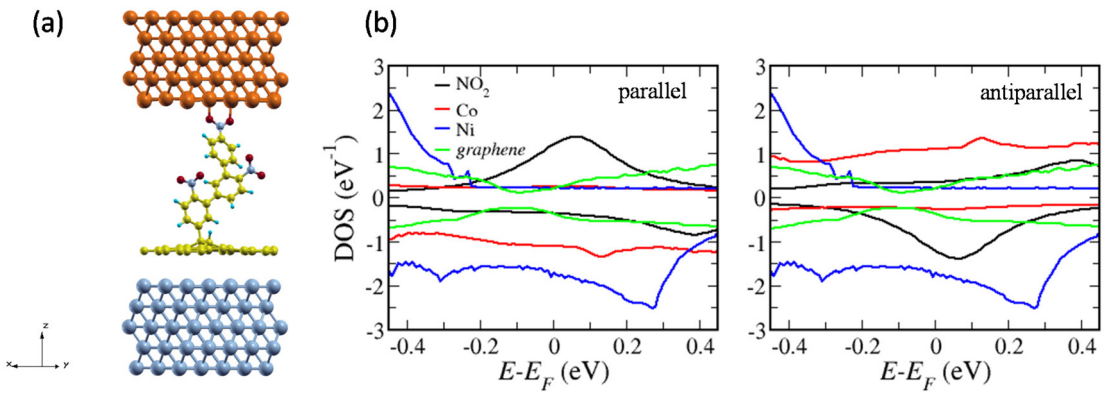

Fig. 5 Theoretical investigation of the interfacial electronic properties. (a) Structure of the hybrid junction used in the calculations. Blue atoms: Ni, yellow atoms: C, light blue atoms: H, red atoms: O, grey atoms: N, orange atoms: Co. (b) DOS projected over a Ni atom (blue line); the molecule topmost NO_2 group (black line), where the LUMO is localized; the Co atom covalently attached to the molecule (red line); the graphene layer (green line). States with a "positive" DOS correspond to the spin-up states whereas the states with a "negative" DOS correspond to a spin down states.

trode,[15] which can reverse the spin-filter properties of the bare electrode like for the well-known LSMO/Alq_3,[13] Co/CoPc,[65] Fe/MnPc[66] and Fe/H_2Pc[67] systems. This feature determines the negative MR at zero bias and also plays an important role at finite bias as discussed in the following.

Combined action of spin-filtering mechanisms

The magnetoresistive response of the system to a finite bias voltage V is simulated by means of the non-equilibrium Green's function (NEGF).[68–71] The current for the parallel (anti-parallel) configuration is obtained from the energy (E)- and V-dependent transmission coefficient, $T_{P(AP)}(E, V)$, as:[68,69]

$$I_{P(AP)} = \frac{e}{h}\int T_{P(AP)}(E,V)[f(E-\mu_b) - f(E-\mu_t)]\mathrm{d}E \qquad (2)$$

where e is the electron charge, h is the Planck's constant, $\mu_b = E_F + eV/2$ ($\mu_t = E_F - eV/2$) is the chemical potential of the bottom (top) electrode, and $f(E)$ is the Fermi function. The MR is then obtained from the P and AP currents using eqn (1). The voltage V is defined in the same way as in experiment so that electrons flow from the top to the bottom electrode for a positive bias (see Fig. 3). We note that, in practice, the integrand in eqn (2) is significantly different from zero only in an energy region extending from approximately $E_F - eV/2$ to $E_F + eV/2$ and called "bias window". Thus, the relative magnitude of the P and AP currents can simply be estimated from the area under the functions $T_P(E, V)$ and $T_{AP}(E, V)$ inside such bias window. The MR will be positive when that area is larger for the P than for the AP configuration. Conversely, the MR will be negative. This analysis is displayed for the in Fig. 6 at three different bias voltages and will be used extensively in the following.

The current I_P calculated with eqn (2) is about 100 pA and 400 pA respectively at ±0.1 V and ±0.2 V in good agreement with the measurements in Fig. 3 thus indicating our structure for the molecular junction is a reliable model representation of the device. The corresponding MR as a function of V is then shown in Fig. 7. It is positive near zero bias, whereas it changes sign at both positive and negative bias voltages as qualitatively observed in the experiments. This is a remarkable finding, which suggests that the switching of the MR sign is a characteristic and robust feature of our devices.

To interpret the results in terms of the underlaying physical effects, we need to relate $T_{P(AP)}(E, V)$ to the electronic structure. Here, we use a general argument and, neglecting quantum interference and symmetry-related effects, we assume that the transmission coefficient is proportional to the system DOS. Effectively, this means that, if the DOS of all stacked materials in a device is large at a certain energy, electrons will be transmitted at that energy. In contrast, the transmission will be reduced in the case that some of the materials have a low DOS as electrons will be blocked by the lack of available conducting

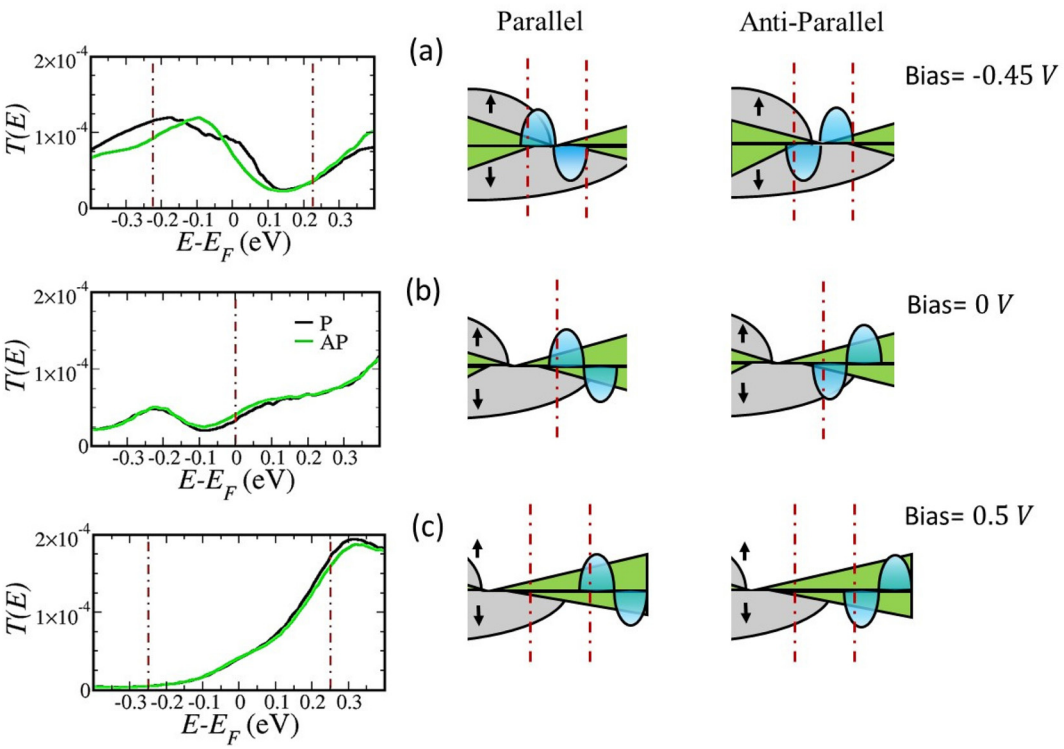

Fig. 6 Spin dependent transmission of the system for different applied bias voltages. Left: transmission coefficient for the parallel (P, black line) and the antiparallel (AP, green line) configurations at −0.45 V (a), 0.0 V (b) and 0.5 V (c). The vertical red dashed lines delimit the bias window eV. Right: cartoon illustrating the bias-induced shift of the DOS for the parallel (left) and antiparallel (right) configurations of the electrodes' magnetizations. The LUMO DOS is colored in cyan, the Ni 3d DOS in grey and the Gr DOS in green. The calculated DOS are presented in the Supp. Info.

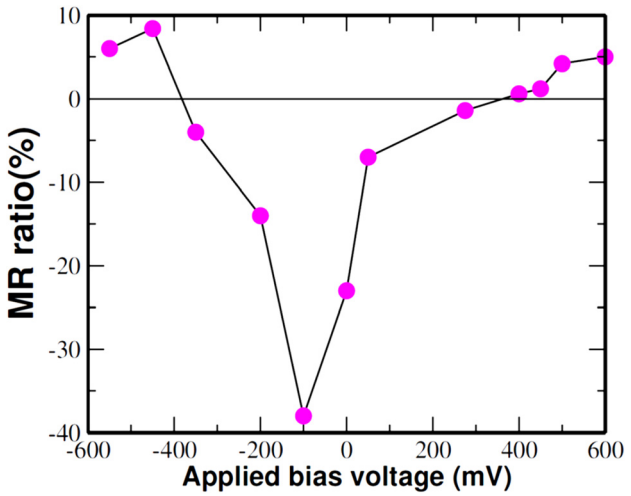

Fig. 7 Calculated MR spin signal. The result is in qualitative agreement with the bias voltage dependent switching of the spin filtering sign observed in experimental junctions as shown in Fig. 4(c).

states. Within this picture, it is important to consider that the DOS of a molecular junction under a finite bias voltage does not remain the same as at zero-bias. Assuming a linear potential drop between the electrodes, the DOS of the bottom (top) electrode of a molecular device is rigidly shifted in energy of –(+)V/2. Effectively, the bias voltage alters the energy level alignment between the various materials of a device and, therefore, the transmission [note that, accordingly, we indicated the transmission coefficient as V-dependent in eqn (2)]. Furthermore, in the case of a device with ferromagnetic electrodes, the bias voltage affects the positions in energy of the majority and minority bands of one electrode with respect to the positions of the molecular orbitals and the positions of the majority and minority bands of the other electrode. In general, this effect can result in a change of the MR magnitude. In our specific Ni/Gr/NB/Co junction, it becomes large enough to reverse the MR sign at certain voltages. The mechanism is analyzed in detail in the following in terms of the DOS. We will compare zero bias, negative bias, and positive bias calculations, and we will highlight the distinct spin-dependent behavior of the three cases. The transmission coefficients are presented in Fig. 6 along with the schematic representation of the corresponding DOS.

Zero-bias. The DOS projected over the different materials of the Ni/Gr/NB/Co junction was analyzed in the previous section (Fig. 5), where we pointed out that the LUMO of the NB unit hybridized with Co acted effectively as a new electrode, called NB LUMO/Co, and as a metallic spin-filter state at E_F. In the device in the parallel magnetic configuration, it filters (*i.e.*, transmits) spin-up electrons, but there are no available conducting spin up states at E_F in the bottom electrode. On the other hand, in the antiparallel magnetic configuration, the LUMO filters spin-down electrons, which can be transmitted into the Ni/Gr electrode as its spin down DOS is large at E_F. As a result, we find that $T_{AP}(E_F, V = 0)$ is larger than $T_P(E_F, V = 0)$, and therefore, the MR ratio near zero-bias is negative like in experiment. In our specific idealized junction, the estimate of the MR ratio is almost −40%, highlighting the strong potential that can be expected from such systems. Although, our results quantitatively depend on several factors, such as the contact geometry and the energy position of the LUMO with respect to E_F, which are difficult to estimate with great accuracy, we stress that the behavior of the LUMO as spin-filter is a solid feature of the system and it fully accounts for the spin-dependent transport properties near zero-bias.

Negative bias voltage. The DOS of the device is drastically modified by the applied bias voltage compared to the zero-bias case as displayed in the schematic representation of Fig. 6(a) (the calculated DOS is presented in Fig. S3†). The Ni/Gr DOS moves towards higher energies by about $|V|/2$, whereas the effective NB LUMO/Co electrode moves towards lower energies by about $-|V|/2$. In the junction parallel magnetic configuration, the spin up and spin down LUMO resonances overlap in energy respectively with the majority and minority Ni/Gr DOS inside the bias window for large enough applied bias voltages. Both spin up and spin down electrons are therefore transmitted from Ni/Gr through the molecule and to the Co. In contrast, in the antiparallel magnetic configuration, the overlap of the spin up NB LUMO DOS with the Ni/Gr spin up DOS is quite small, and, therefore, spin up electrons are not transmitted. Only spin down electrons are transmitted. As a result, the area under the total transmission curve inside the bias window is larger in the parallel than in the antiparallel configuration, and the MR is positive.

Positive bias voltage. The NB LUMO moves towards higher energies by about $|V|/2$ with respect to the zero-bias case. It leaves the bias window becoming irrelevant for transport in one spin channel, while it remains partly inside the bias window in the opposite spin-channel as sketched in Fig. 6(c). As a consequence, in the parallel (antiparallel) magnetic configuration, the effective top NB LUMO/Co electrode filters spin up (down) electrons, or in other words, electrons coming from the top electrode acquire a positive (negative) spin polarization. On the other hand, at the bottom electrode, the Ni/Gr DOS moves down in energy by about $-|V|/2$ with respect to the zero-bias case. For a large enough voltage, the 3d Ni states exit the bias window, whereas the Gr conduction band enters. This Gr conduction band has a positive spin polarization inside the bias window owing to the hybridization with Ni (see Fig. S2†). Therefore, the spin polarization of the bottom electrode has the same (opposite) sign as (with respect to) the spin polarization of the effective top electrode in the parallel (antiparallel) configuration. Electron flow is (dis-) favored in the (anti-) parallel configuration, and the MR is positive.

While the proposed model explains qualitatively the bias voltage-induced modulation of the spin transport properties, as previously discussed in the molecular electronics field,[72,73] achieving a quantitative agreement (such as with the asymmetry, the magnitude of the zero-bias MR and of the switching bias) is more complex as was even shown in the simplest single molecule case.[55,74]

Conclusions

Our work demonstrates that electrografted organic films can be successfully integrated in spintronic devices by introducing a graphene passivation layer by CVD serving as a platform for electrografting of organic molecules. We illustrated this possibility focusing on reference organic NB oligomeric chains. Our approach led to the observation of a MR signal attributed to spin transport confirming that spin sources are indeed not quenched during our new fabrication approach. Furthermore, we showed that the spin signal could be switched in sign *via* the bias voltage tuning the tunneling of majority and minority spin carriers across the device. The complementary experimental findings which demonstrate that the origin of the MR is a result from the molecular structure are:

• the absence of sign change in the MR effect in devices made of Ni/graphene/Al_2O_3/Co[28] and in Ni/graphene/Co,[62]

• the absence of any MR effects in Au (50 nm)/NB (1.3 nm)/Co (15 nm) junctions (see Fig. S1†).

This filtering effect translates into a new functionality specific to our device set-up and which has not been reported in other spintronic devices. Supported by first-principles calculations, we proposed a microscopic mechanism, and we uncovered the combined role of the molecule/ferromagnetic metal and of the graphene/ferromagnetic metal interfaces for spin-filtering. Although our measurements were carried out at low temperatures, a further improvement of the fabrication technique and the selection of different organic chains aided by first-principles theoretical predictions might boost the device performance toward higher temperatures in future experiments by searching, for instance, for stronger spin filtering effects and level energetics compatible with room temperature experiments. Furthermore, spintronic properties could be combined with other previously reported effects such as rectification[39,55] and enhanced Seebeck effect[75] characteristic of the molecule-graphene covalent contact thus exploring truly multifunctional behaviors. Our work is an early step, but it opens the perspective for chemical tailoring using electrochemistry methods towards the realization of the next generation of molecular spintronic devices.

Methods

Hybrid spin-valves fabrication. Bottom Ni electrodes are fabricated by e-beam lithography using UVIII resist on a SiO_2(90 nm)/Si substrate and subsequent sputtering of Ni and lift-off. After the graphene passivation layer integration by CVD and the electrochemistry step, micro-junctions are defined in a second e-beam step. 5 μm × 5 μm windows were opened in UVIII resist on top of grafted Ni/Gr.[28] The top electrode (Co (15 nm)/Au (50 nm)) is finally deposited by evaporation at a rate of 0.05 nm s^{-1} and at a pressure of 10^{-7} mBar. This overall defines a full hybrid spin-valve encompassing the graphene/NB spacer.

Graphene passivation layer integration. The graphene passivation layer is grown in a cold-wall CVD system.[28,30,31] The Ni stripes are first heated to 600 °C (at 300 °C min^{-1}) in a H_2 atmosphere (100 Pa) and annealed for 15 min. They are then exposed to 1 Pa C_2H_2 for another 15 min. Finally, they are cooled down in vacuum at 100 °C min^{-1}. This growth results in a few-layer graphene coating.[28,30,31]

Electrochemistry step for molecular chain grafting. All electrochemical experiments were carried out with a conventional three-electrode cell with a classical potentiostat (@CH Instruments). The potential was measured with a saturated calomel electrode (SCE) and a counter-electrode (stainless steel grid). Working electrodes were glassy carbon from CH Instrument or Ni/Gr provided by CVD process. The electrolyte (tetra-butyl ammonium tetrafluoroborate, Bu_4NBF_4) and the diazonium salt, 4-nitrophenyldiazonium tetrafluoroborate, were purchased from Sigma Aldrich and used as received. All solutions were freshly prepared in distilled acetonitrile (ACN). A NBD (0.5 mM) solution with 0.1 M supporting electrolyte was prepared and degassed for at least 5 min to remove oxygen, and reduction was carried out by successive potential sweeps at a scan rate of 100 mV s^{-1}, leading to oligomer films, with thicknesses from 2 to 10 nm, grafted onto various electrodes. The modified electrodes were removed from the solution, rinsed with ACN to remove weakly adsorbed molecules.

Magneto-transport measurement setup. The measurement setup is a standard DC current–voltage characterization in which the measured current is amplified by a low-noise *I–V* converter. The results presented were obtained in an Oxford Instruments SM 4000-8 cryostat (T = 1.5 K, $P \approx 10^{-5}$ mbar).

Interfacial chemical analysis by XPS. XPS spectra are acquired using an Omicron NanoTechnology GmbH system with a base pressure of 5 × 10^{-10} mbar, and using a Mg Kα source (hv = 1253.6 eV) operating at 20 mA and 15 kV. Spectral analysis is carried out with the CasaXPS software (CasaSoftware Ltd). The XPS measurements are performed *ex situ* and show the preservation of the metallic nature of Ni after graphene growth and electrochemistry steps.

Structure and optimization of model device. We consider a supercell containing three layers of Ni and Co. Gr is adsorbed on Ni in the so-called "atop site/hcp site"[63] as there is experimental evidence that this is the most likely configuration in our experiments.[62] A single NB molecule is chemisorbed on Gr forming a sp^3 bond at the adsorption site. This is accompanied by a dangling bond at the nearest neighbor site. However, experiments indicate the formation of a very dense film. Dangling bonds are likely saturated by other molecules due to their high reactivity.[76] To remove the dangling bond in our calculations we add an H atom. As discussed in detail in a previous works,[55] there is no difference in the computed interface electronic structure whether the dangling bond is passivated by another molecule or by H. The Gr/Ni separation is set according to the literature equal to the physisorption distance $d_{\mathrm{Ni/graphene}}$ = 3.3 Å calculated with the Random Phase Approximation in ref. 61. For the top electrode we assume Co to have *fcc* structure like Ni and the electrode to terminate with a flat (111) surface. We note that using, for instance, a tip-like electrode would affect quantitatively, but not qualitatively the results and the phenomenology presented in our work.

The interface atomic structures are optimized using the Fritz Haber Institute *ab initio* molecular simulations (FHI-aims) DFT all-electron code.[77] The standard numerical atom-centered orbitals basis sets "tier 1" and "tier 2" are considered for Ni and H, C, N and O respectively. We use the Perdew–Burke–Ernzerhof generalized gradient approximation[78] for the exchange–correlation functional as it accurately describes both the molecule/Gr and the molecule/Co covalent chemical bonds between. For the structural optimizations, we fix the bottom Ni and top Co layer and let the other atoms relax until force are smaller than 0.01 eV per Ang. Furthermore, we constrain the Gr–Ni separation as DFT with PBE does not account for physisorption in Gr/Ni. All other atoms are relaxed to forces below 0.01 eV $Å^{-1}$. A 4 × 8 *k*-point mesh was used, and all calculations are spin-polarized.

Quantum transport calculations. Electron transport calculations are carried out with the Smeagol code,[68] which combines the NEGF method with DFT as implemented in the Siesta package.[79] The junction is effectively infinite along the *z* transport direction with the top and bottom electrode described by means of embedding self-energies,[80] while a rectangular 4 × 2 supercell was considered in the *xy* plane. We use a double-ζ plus polarization basis set for all atoms. We treat core electrons with norm-conserving Troullier–Martin pseudopotentials, and we use the local spin density approximation (LSDA) for the exchange–correlation functional.[81] The real-space mesh was set by an equivalent energy cutoff of 400 Ry. We find that the density matrix is converged for 4 × 8 *k*-points. The transmission is then calculated for a given converged charge density with a finer 48 × 96 *k*-point mesh to better resolve the energy-region near the Gr Dirac cone. At the low bias voltages considered here the molecule conducts in the tunneling regime and does not change its charging state. We therefore perform the finite bias out-of-equilibrium calculations for the evaluation of the current non-self-consistently adding a potential ramp between the Co top electrode and Ni/Gr bottom electrode to the equilibrium potential.[55]

DFT within the LSDA generally places unoccupied states too low in energy. The calculated conductance and current then show a too sharp increase already at voltages as small as 0.1 V as electrons are predicted to tunnel not just through the LUMO, but also through the LUMO+1 and LUMO+2. The LUMO+1 and the LUMO+2 are localized on the central and bottom unit of the molecular chain and they are not hybridized with the Co top electrode. We therefore add a scissor operator correction for these states to evaluate the transmission.[82,83] A correction larger than 0.4 eV is enough to push unoccupied molecular orbitals other than the LUMO outside the considered bias windows thus recovering a much better agreement with experiments. Similarly, we also apply a small rigid shift to the DOS of the Ni/Gr bottom electrode. Our calculations predict that the Gr Dirac code is in energy at about 0.25 eV below the Fermi level. Consequently, the conductance minimum is not at 0 V in disagreement with experiments. We find that the conductance minimum shifts towards 0 V when the Dirac cone is positioned at 0.1 eV below the Fermi level.

Author contributions

A.D. performed all the theoretical analysis. P.M. and L.C. performed the electrografting of molecules. B.D., M.-B.M, P.S., R. M., F.G., A.S. and S.C. performed the growth and characterizations of Ni/graphene bilayers. P.M., B.D. and C.B. performed the device fabrication and the magnetotransport experiments. C.B., P.L., T.H., M.-L.D.L, and F.M. performed the electrical characterization of the devices. All the authors have contributed to the general discussion.

Conflicts of interest

There are no conflicts to declare.

Acknowledgements

C.B. and P.M. acknowledge P. Filloux for his technical support within the cleanroom facility of the Laboratoire Matériaux et Phénomènes Quantiques (UMR 7162). C.B. and P.M. also acknowledge R. Bonnet and J. Rastikian for their help during the electrical characterizations. C.B. acknowledges financial support from the Ville de Paris "Emergence" program ("2DSPIN" project) and from the "Région Ile-de-France" in the framework of DIM Nano-K through the research project "Spin transport at the Molecular Scale" project. This project has also received funding from the European Union's H2020 Future and Emerging Technologies Graphene Flagship (Grant Core3 No. 881603). This research is supported by a public grant overseen by the French National Research Agency (ANR) as part of the "Investissements d'Avenir" program Labex NanoSaclay (ANR-10-LABX- 0035), as well as grants MIXES (ANR-19-CE09-0028) and STEM2D (ANR-19-CE24-0015). A.D. acknowledges funding by the Science Foundation Ireland (SFI) and the Royal Society through the University Research Fellowship URF-R1-191769. Computational resources were provided by Trinity College Dublin Research IT.

References

1 A. V. Khvalkovskiy, D. Apalkov, S. Watts, R. Chepulskii, R. S. Beach, A. Ong, X. Tang, A. Driskill-Smith, W. H. Butler, P. B. Visscher, D. Lottis, E. Chen, V. Nikitin and M. Krounbi, *J. Phys. D: Appl. Phys.*, 2013, **46**, 074001.

2 B. Dieny, I. L. Prejbeanu, K. Garello, P. Gambardella, P. Freitas, R. Lehndorff, W. Raberg, U. Ebels, S. O. Demokritov, J. Akerman, A. Deac, P. Pirro, C. Adelmann, A. Anane, A. V. Chumak, A. Hirohata, S. Mangin, S. O. Valenzuela, M. C. Onbaşlı, M. D'Aquino, G. Prenat, G. Finocchio, L. Lopez-Diaz, R. Chantrell, O. Chubykalo-Fesenko and P. Bortolotti, *Nat. Electron.*, 2020, **3**, 446–459.

3 D. Saida, S. Kashiwada, M. Yakabe, T. Daibou, M. Fukumoto, S. Miwa, Y. Suzuki, K. Abe, H. Noguchi, J. Ito

and S. Fujita, *IEEE Trans. Electron Devices*, 2017, **64**, 427–431.
4 B. Behin-Aein, D. Datta, S. Salahuddin and S. Datta, *Nat. Nanotechnol.*, 2010, **5**, 266–270.
5 W. A. Borders, A. Z. Pervaiz, S. Fukami, K. Y. Camsari, H. Ohno and S. Datta, *Nature*, 2019, **573**, 390–393.
6 S. Manipatruni, D. E. Nikonov, C.-C. Lin, T. A. Gosavi, H. Liu, B. Prasad, Y.-L. Huang, E. Bonturim, R. Ramesh and I. A. Young, *Nature*, 2019, **565**, 35–42.
7 J. Grollier, D. Querlioz, K. Y. Camsari, K. Everschor-Sitte, S. Fukami and M. D. Stiles, *Nat. Electron.*, 2020, **3**, 360–370.
8 M. Piquemal-Banci, R. Galceran, M.-B. Martin, F. Godel, A. Anane, F. Petroff, B. Dlubak and P. Seneor, *J. Phys. D: Appl. Phys.*, 2017, **50**, 203002.
9 P. Seneor, B. Dlubak, M.-B. Martin, A. Anane, H. Jaffres and A. Fert, *MRS Bull.*, 2012, **37**, 1245–1254.
10 D. Li and G. Yu, *Adv. Funct. Mater.*, 2021, **31**, 2100550.
11 S. Delprat, M. Galbiati, S. Tatay, B. Quinard, C. Barraud, F. Petroff, P. Seneor and R. Mattana, *J. Phys. D: Appl. Phys.*, 2018, **51**, 473001.
12 V. Dediu, M. Murgia, F. C. C. Matacotta, C. Taliani and S. Barbanera, *Solid State Commun.*, 2002, **122**, 181–184.
13 Z. H. Xiong, D. Wu, Z. V. Vardeny and J. Shi, *Nature*, 2004, **427**, 821–824.
14 T. S. Santos, J. S. Lee, P. Migdal, I. C. Lekshmi, B. Satpati and J. S. Moodera, *Phys. Rev. Lett.*, 2007, **98**, 016601.
15 C. Barraud, P. Seneor, R. Mattana, S. Fusil, K. Bouzehouane, C. Deranlot, P. Graziosi, L. Hueso, I. Bergenti, V. Dediu, F. Petroff and A. Fert, *Nat. Phys.*, 2010, **6**, 615–620.
16 M. Cinchetti, V. A. Dediu and L. E. Hueso, *Nat. Mater.*, 2017, **16**, 507–515.
17 Y. Q. Zhan, X. J. Liu, E. Carlegrim, F. H. Li, I. Bergenti, P. Graziosi, V. Dediu and M. Fahlman, *Appl. Phys. Lett.*, 2009, **94**, 053301.
18 J. Pinson and F. Podvorica, *Chem. Soc. Rev.*, 2005, **34**, 429–439.
19 D. Bélanger and J. Pinson, *Chem. Soc. Rev.*, 2011, **40**, 3995–4048.
20 J. R. Petta, S. K. Slater and D. C. Ralph, *Phys. Rev. Lett.*, 2004, **93**, 136601.
21 W. Wang and C. A. Richter, *Appl. Phys. Lett.*, 2006, **89**, 153105.
22 Z. Mekhalif, J. Riga, J.-J. Pireaux and J. Delhalle, *Langmuir*, 1997, **13**, 2285–2290.
23 M. Galbiati, S. Delprat, M. Mattera, S. Mañas-Valero, A. Forment-Aliaga, S. Tatay, C. Deranlot, P. Seneor, R. Mattana and F. Petroff, *AIP Adv.*, 2015, **5**, 057131.
24 H. Vinzelberg, J. Schumann, D. Elefant, R. B. Gangineni, J. Thomas and B. Büchner, *J. Appl. Phys.*, 2008, **103**, 093720.
25 J. S. S. Moodera, L. R. Kinder, T. M. Wong and R. Meservey, *Phys. Rev. Lett.*, 1995, **74**, 3273–3276.
26 T. Fluteau, C. Bessis, C. Barraud, M. L. Della Rocca, P. Martin, J.-C. Lacroix and P. Lafarge, *J. Appl. Phys.*, 2014, **116**, 114509.
27 Q. van Nguyen, P. Martin, D. Frath, M. L. Della Rocca, F. Lafolet, C. Barraud, P. Lafarge, V. Mukundan, D. James, R. L. McCreery and J.-C. Lacroix, *J. Am. Chem. Soc.*, 2017, **139**, 11913–11922.
28 B. Dlubak, M.-B. B. Martin, R. S. Weatherup, H. Yang, C. Deranlot, R. Blume, R. Schloegl, A. Fert, A. Anane, S. Hofmann, P. Seneor and J. Robertson, *ACS Nano*, 2012, **6**, 10930–10934.
29 P. Z. Sun, Q. Yang, W. J. Kuang, Y. V. Stebunov, W. Q. Xiong, J. Yu, R. R. Nair, M. I. Katsnelson, S. J. Yuan, I. V. Grigorieva, M. Lozada-Hidalgo, F. C. Wang and A. K. Geim, *Nature*, 2020, **579**, 229–232.
30 R. S. Weatherup, B. Dlubak and S. Hofmann, *ACS Nano*, 2012, **6**, 9996–10003.
31 H. Naganuma, V. Zatko, M. Galbiati, F. Godel, A. Sander, C. Carrétéro, O. Bezencenet, N. Reyren, M.-B. Martin, B. Dlubak and P. Seneor, *Appl. Phys. Lett.*, 2020, **116**, 173101.
32 G. L. C. Paulus, Q. H. Wang and M. S. Strano, *Acc. Chem. Res.*, 2013, **46**, 160–170.
33 S. Niyogi, E. Bekyarova, M. E. Itkis, H. Zhang, K. Shepperd, J. Hicks, M. Sprinkle, C. Berger, C. N. Lau, W. A. deHeer, E. H. Conrad and R. C. Haddon, *Nano Lett.*, 2010, **10**, 4061–4066.
34 M. Delamar, R. Hitmi, J. Pinson and J. M. Saveant, *J. Am. Chem. Soc.*, 1992, **114**, 5883–5884.
35 J. Ghilane, P. Martin, O. Fontaine, J.-C. Lacroix and H. Randriamahazaka, *Electrochem. Commun.*, 2008, **10**, 1060–1063.
36 R. J. Cullen, D. R. Jayasundara, L. Soldi, J. J. Cheng, G. Dufaure and P. E. Colavita, *Chem. Mater.*, 2012, **24**, 1031–1040.
37 S. S. C. Yu, E. S. Q. Tan, R. T. Jane and A. J. Downard, *Langmuir*, 2007, **23**, 11074–11082.
38 J. L. Bahr, J. Yang, D. V. Kosynkin, M. J. Bronikowski, R. E. Smalley and J. M. Tour, *J. Am. Chem. Soc.*, 2001, **123**, 6536–6542.
39 C. Barraud, M. Lemaitre, R. Bonnet, J. Rastikian, C. Salhani, S. Lau, Q. van Nguyen, P. Decorse, J.-C. Lacroix, M. L. Della Rocca, P. Lafarge and P. Martin, *Nanoscale Adv.*, 2019, **1**, 414–420.
40 P. Martin, M. L. Della Rocca, A. Anthore, P. Lafarge and J.-C. Lacroix, *J. Am. Chem. Soc.*, 2012, **134**, 154–157.
41 D. Bouilly, J. Cabana, F. Meunier, M. Desjardins-Carrière, F. Lapointe, P. Gagnon, F. L. Larouche, E. Adam, M. Paillet and R. Martel, *ACS Nano*, 2011, **5**, 4927–4934.
42 R. Bonnet, P. Martin, S. Suffit, P. Lafarge, A. Lherbier, J. C. Charlier, M. L. Della Rocca and C. Barraud, *Sci. Adv.*, 2020, **6**, eaba5494.
43 V. Stockhausen, J. Ghilane, P. Martin, G. Trippé-Allard, H. Randriamahazaka and J.-C. Lacroix, *J. Am. Chem. Soc.*, 2009, **131**, 14920–14927.
44 J. Pinson and F. I. Podvorica, *Curr. Opin. Electrochem.*, 2020, **24**, 44–48.
45 J. C. Lacroix, G. Trippe-Allard, J. Ghilane and P. Martin, *Adv. Nat. Sci.: Nanosci. Nanotechnol.*, 2013, **5**, 015001.

46 S. Y. Sayed, J. A. Fereiro, H. Yan, R. L. Mccreery, A. Johan, A. J. Bergren and A. Johan, *Proc. Natl. Acad. Sci. U. S. A.*, 2012, **109**, 11498–11503.
47 H. Yan, A. J. Bergren and R. L. McCreery, *J. Am. Chem. Soc.*, 2011, **133**, 19168–19177.
48 H. Yan, A. J. Bergren, R. McCreery, M. L. Della Rocca, P. Martin, P. Lafarge and J.-C. C. Lacroix, *Proc. Natl. Acad. Sci. U. S. A.*, 2013, **110**, 5326–5330.
49 S. M. Park, H. Yu, M. G. Park, S. Y. Han, S. W. Kang, H. M. Park and J. W. Kim, *Surf. Interface Anal.*, 2012, **44**, 156–161.
50 M. P. Seah and W. A. Dench, *Surf. Interface Anal.*, 1979, **1**, 2–11.
51 U. Rüdiger, R. Calarco, U. May, K. Samm, J. Hauch, H. Kittur, M. Sperlich and G. Güntherodt, *J. Appl. Phys.*, 2001, **89**, 7573–7575.
52 S. Tatay, M. Galbiati, S. Delprat, C. Barraud, K. Bouzehouane, S. Collin, C. Deranlot, E. Jacquet, P. Seneor, R. Mattana and F. Petroff, *J. Phys.: Condens. Matter*, 2016, **28**, 94010.
53 S. Tatay, C. Barraud, M. Galbiati, P. Seneor, R. Mattana, K. Bouzehouane, C. Deranlot, E. Jacquet, A. Forment-Aliaga, P. Jegou, A. Fert and F. Petroff, *ACS Nano*, 2012, **6**, 8753–8757.
54 Z. Mekhalif, J. Delhalle, J.-J. Pireaux, S. Noël, F. Houzé and L. Boyer, *Surf. Coat. Technol.*, 1998, **100–101**, 463–468.
55 A. V. Rudnev, V. Kaliginedi, A. Droghetti, H. Ozawa, A. Kuzume, M. Aki Haga, P. Broekmann and I. Rungger, *Sci. Adv.*, 2017, **3**, e1602297.
56 M. B. Martin, B. Dlubak, R. S. Weatherup, H. Yang, C. Deranlot, K. Bouzehouane, F. Petroff, A. Anane, S. Hofmann, J. Robertson, A. Fert and P. Seneor, *ACS Nano*, 2014, **8**, 7890–7895.
57 A. Forment-Aliaga and E. Coronado, *Chem. Rec.*, 2018, **18**, 737–748.
58 M. Jullière, *Phys. Lett. A*, 1975, **54**, 225–226.
59 S. Sanvito, *Nat. Phys.*, 2010, **6**, 562–564.
60 S. Sanvito, *Nature*, 2010, **467**, 664–665.
61 F. Mittendorfer, A. Garhofer, J. Redinger, J. Klimeš, J. Harl and G. Kresse, *Phys. Rev. B: Condens. Matter Mater. Phys.*, 2011, **84**, 201401.
62 M. Piquemal-Banci, R. Galceran, S. M.-M. Dubois, V. Zatko, M. Galbiati, F. Godel, M.-B. Martin, R. S. Weatherup, F. Petroff, A. Fert, J.-C. Charlier, J. Robertson, S. Hofmann, B. Dlubak and P. Seneor, *Nat. Commun.*, 2020, **11**, 5670.
63 A. Dahal and M. Batzill, *Nanoscale*, 2014, **6**, 2548–2562.
64 V. M. Karpan, G. Giovannetti, P. A. Khomyakov, M. Talanana, A. A. Starikov, M. Zwierzycki, J. van den Brink, G. Brocks and P. J. Kelly, *Phys. Rev. Lett.*, 2007, **99**, 176602.
65 C. Barraud, K. Bouzehouane, C. Deranlot, S. Fusil, H. Jabbar, J. Arabski, R. Rakshit, D.-J. J. Kim, C. Kieber, S. Boukari, M. Bowen, E. Beaurepaire, P. Seneor, R. Mattana and F. Petroff, *Phys. Rev. Lett.*, 2015, **114**, 206603.
66 F. Djeghloul, M. Gruber, E. Urbain, D. Xenioti, L. Joly, S. Boukari, J. Arabski, H. Bulou, F. Scheurer, F. Bertran, P. Le Fèvre, A. Taleb-Ibrahimi, W. Wulfhekel, G. Garreau, S. Hajjar-Garreau, P. Wetzel, M. Alouani, E. Beaurepaire, M. Bowen and W. Weber, *J. Phys. Chem. Lett.*, 2016, **7**, 2310–2315.
67 N. Atodiresei, J. Brede, P. Lazić, V. Caciuc, G. Hoffmann, R. Wiesendanger and S. Blügel, *Phys. Rev. Lett.*, 2010, **105**, 066601.
68 A. R. Rocha, V. M. García-Suárez, S. Bailey, C. Lambert, J. Ferrer and S. Sanvito, *Phys. Rev. B: Condens. Matter Mater. Phys.*, 2006, **73**, 085414.
69 I. Rungger, A. Droghetti and M. Stamenova, in *Handbook of Materials Modeling*, eds. W. Andreoni and S. Yip, Springer International Publishing, Cham, 2018, pp. 1–27.
70 J. Taylor, H. Guo and J. Wang, *Phys. Rev. B: Condens. Matter Mater. Phys.*, 2001, **63**, 245407.
71 M. Brandbyge, J.-L. Mozos, P. Ordejón, J. Taylor and K. Stokbro, *Phys. Rev. B: Condens. Matter Mater. Phys.*, 2002, **65**, 165401.
72 F. Evers, R. Korytár, S. Tewari and J. M. Van Ruitenbeek, *Rev. Mod. Phys.*, 2020, **92**, 035001.
73 M. Thoss and F. Evers, *J. Chem. Phys.*, 2018, **148**, 030901.
74 M. Koepf, C. Koenigsmann, W. Ding, A. Batra, C. F. A. Negre, L. Venkataraman, G. W. Brudvig, V. S. Batista, C. A. Schmuttenmaer and R. H. Crabtree, *Nanoscale*, 2016, **8**, 16357–16362.
75 A. Droghetti and I. Rungger, *Phys. Chem. Chem. Phys.*, 2020, **22**, 1466–1474.
76 S. Goler, C. Coletti, V. Tozzini, V. Piazza, T. Mashoff, F. Beltram, V. Pellegrini and S. Heun, *J. Phys. Chem. C*, 2013, **117**, 11506–11513.
77 V. Blum, R. Gehrke, F. Hanke, P. Havu, V. Havu, X. Ren, K. Reuter and M. Scheffler, *Comput. Phys. Commun.*, 2009, **180**, 2175–2196.
78 J. P. Perdew, K. Burke and M. Ernzerhof, *Phys. Rev. Lett.*, 1996, **77**, 3865.
79 J. M. Soler, E. Artacho, J. D. Gale, A. García, J. Junquera, P. Ordejón and D. Sánchez-Portal, *J. Phys.: Condens. Matter*, 2002, **14**, 2745–2779.
80 I. Rungger and S. Sanvito, *Phys. Rev. B*, 2008, **78**, 035407.
81 U. von Barth and L. Hedin, *J. Phys. C: Solid State Phys.*, 1972, **5**, 1629.
82 A. de M. Souza, I. Rungger, R. B. Pontes, A. R. Rocha, A. J. R. da Silva, U. Schwingenschlöegl and S. Sanvito, *Nanoscale*, 2014, **6**, 14495–14507.
83 A. Droghetti and I. Rungger, *Phys. Rev. B*, 2017, **95**, 085131.

